

RESEARCH ARTICLE

10.1002/2013JD021347

Key Points:

- Distinct wave-cloud lines are observed over the Arabian Sea
- The associated convergence lines are visible in an ERA-I climatology
- Formation mechanism is associated with the sea breeze

Correspondence to:

C. E. Birch,
C.E.Birch@leeds.ac.uk

Citation:

Birch, C. E., M. J. Reeder, and G. J. Berry (2014), Wave-cloud lines over the Arabian Sea, *J. Geophys. Res. Atmos.*, 119, 4447–4457, doi:10.1002/2013JD021347.

Received 11 DEC 2013

Accepted 19 MAR 2014

Accepted article online 21 MAR 2014

Published online 16 APR 2014

Wave-cloud lines over the Arabian Sea

C. E. Birch^{1,2}, M. J. Reeder^{3,4}, and G. J. Berry³

¹Institute for Climate and Atmospheric Science, University of Leeds, Leeds, UK, ²Now at UK Met Office, Leeds, University of Leeds, UK, ³School of Mathematical Sciences, Monash University, Clayton, Victoria, Australia, ⁴Centre of Excellence for Climate System Science, Monash University, Clayton, Victoria, Australia

Abstract Meteosat visible satellite images between 2006 and 2011 show wave-cloud lines over the Arabian Sea in all months outside the summer monsoon (June–September). These lines are most frequent between January and May (2–3 per month in a given year). All wave-cloud lines in the region propagate offshore. As these wave-cloud lines are associated with coherent convergence lines, the objective technique described by Berry and Reeder is applied to the ERA-Interim reanalysis and a climatology of convergence lines at 850 hPa developed. Despite the coarse resolution of the ERA-Interim reanalysis, the statistical properties of these lines are broadly constant with those deduced from the Meteosat visible satellite images. The generation mechanism is investigated in a simulation with the Met Office Unified Model of a particular wave-cloud line (12 March 2011). The process appears to be similar to that over northwestern Australia, which has been documented previously. During the day, a synoptic-scale northeasterly flow opposes the inland advection of the sea breeze on the west coast of India. However, as the daytime turbulence decays and the boundary layer stabilizes, the northeasterly flow accelerates, pushing offshore the leading edge of the sea breeze during the late evening and early hours of the morning. A wave is generated as the northeasterlies penetrate the marine boundary layer, and this wave propagates westward, producing cloud at its leading edge where there is strong ascent.

1. Introduction

Although few climatologies exist, large-amplitude internal waves, such as solitary waves and internal bores, are thought to be common in the lower atmosphere [e.g., Nudelman *et al.*, 2010; Birch and Reeder, 2012]. Occasionally, clouds mark the crests of these waves. In such cases, moist air is lifted adiabatically in the crest of the approaching wave, producing cloud in otherwise cloud-free regions [e.g., Clarke, 1972; Clarke *et al.*, 1981; Christie, 1992; Smith, 1986; Reeder and Smith, 1998]. At times, the upward displacement of low-level air can play a role in the initiation and organization of convection [e.g., Bosart and Sanders, 1986; Mapes, 1993; Koch and Golus, 1988; Powers and Reed, 1993; Bosart *et al.*, 1998; Koch *et al.*, 2008]. The wind squalls that are produced by large-amplitude internal waves are a potential hazard to low-flying aircraft [Christie and Muirhead, 1983].

Perhaps the most predictable and best documented type of large-amplitude internal wave in the atmosphere is the “Morning Glory,” which occurs regularly in the Gulf of Carpentaria in northeast Australia [Clarke, 1972; Clarke *et al.*, 1981; Christie, 1992; Smith, 1986; Reeder and Smith, 1998; Reeder *et al.*, 2013]. There are several different forms of the wave, with the most common developing over the Cape York Peninsula and propagating toward the southwest [Clarke *et al.*, 1981]. Sea breezes, which form on the westside and eastside of the peninsula, penetrate inland and can collide. When the prevailing easterly wind is relatively weak, the east coast sea breeze is comparable to the west coast sea breeze in strength and depth. In this case, the two sea breezes can collide violently producing large-amplitude disturbances that propagate both upstream and downstream [Reeder *et al.*, 2013]. When the prevailing easterly wind is relatively strong, the east coast sea breeze is usually deeper than the west coast sea breeze, and thus, when the two collide, the easterly sea breeze overrides the westerly sea breeze [Reeder *et al.*, 2013]. A disturbance forms initially at the leading edge of the easterly sea breeze [Goler and Reeder, 2004], which can amplify into bore-like solitary waves that propagate toward the southwest across the Gulf.

Wave-cloud lines have also been identified from satellite imagery over the ocean to the northwest of Australia [Neal and Butterworth, 1973; Clarke *et al.*, 1981] and have been photographed from ships in the region [Smith, 1986]. Birch and Reeder [2012] show from satellite imagery that these waves occur at least 2–3 times per month

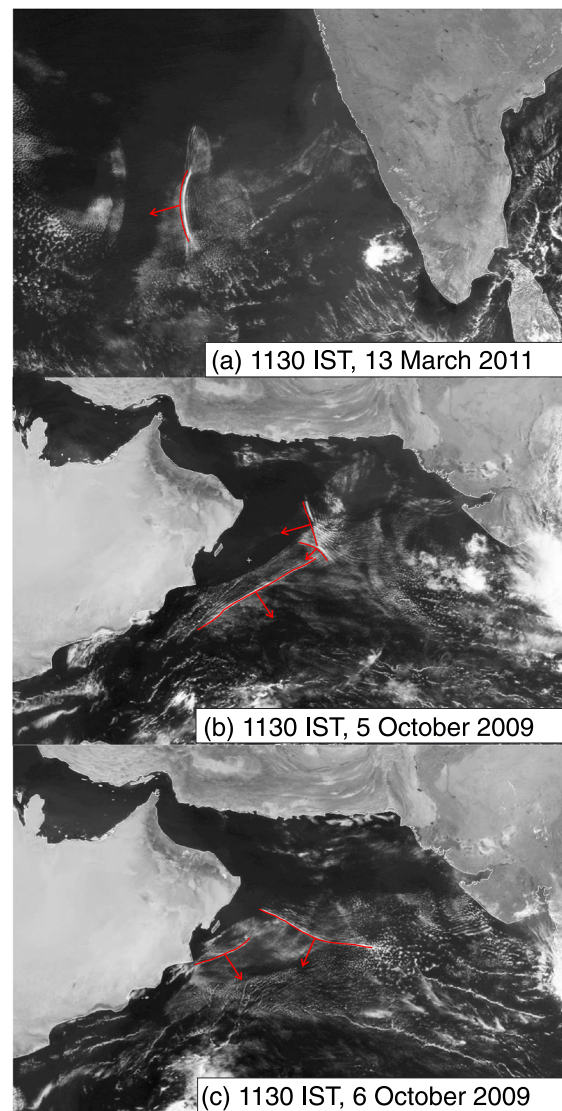


Figure 1. Visible satellite imagery from Meteosat at (a) 1130 IST, 13 March 2011, (b) 1130 IST, 5 October 2009, and (c) 1130 IST, 6 October 2009. The red lines mark the leading edge of the waves, and the red arrows point in the direction of travel (i.e., away from the coastlines).

The present paper uses satellite imagery to identify wave–cloud lines over the Arabian Sea and to construct a climatology of the frequency of occurrence and direction of travel of the waves (section 2). A method for identifying convergence lines in low-resolution gridded data is introduced and is applied to the ERA-Interim reanalysis to construct a climatology of propagating convergence lines in the Arabian Sea (section 3). A case study, similar to the waves observed by Szantai *et al.* [2011], is selected, and a limited-area model simulation is performed to identify the formation mechanism and document the evolution of the wave (sections 4 and 5).

2. Examples of Wave-Cloud Lines and Climatology

Figure 1 shows visible satellite imagery over the Arabian Sea from Meteosat at (a) 1130 Indian Standard Time (IST), 13 March 2011, (b) 1130 IST, 5 October 2009, and (c) 1130 IST, 6 October 2009 (IST = UTC + 0530 h). The leading edges of the waves are marked by the red lines, and the direction of travel by the red arrows. This imagery details some of the best examples of wave clouds observed by the satellite between 2006 and 2011. In all three cases the leading wave is the most distinct and is followed by a series of less pronounced waves of

and use high-resolution, limited-area model simulations to investigate the formation and propagation mechanisms. They conclude that the waves occur in low-level offshore southeasterly flow, which accelerates in the evening and collides with the onshore sea breeze. The southeasterlies override the sea breeze, and the wave–cloud lines form at the leading edge of the offshore flow, propagating along an elevated inversion layer that caps the well-mixed marine boundary layer.

Similar wave clouds have been identified in the Mozambique Channel in the southwest Indian Ocean [da Silva and Magalhães, 2009] and also over the north Indian Ocean. Zheng *et al.* [1998] present a wave identified from Space Shuttle images which appears to originate from the Pakistani coast and propagate southward. The wave is very similar in appearance to the wave–clouds described in Birch and Reeder [2012]. Szantai *et al.* [2011] observed solitary waves on a number of days from a ship in the Arabian Sea during the Indian Ocean Experiment between January and March 1999. They tracked these waves using satellite imagery and found that they traveled westward at speeds of $10\text{--}18\text{ m s}^{-1}$ and lasted for up to 48 h. They suggest that the inversion layer above the marine boundary layer may have acted as a waveguide, thereby explaining the longevity of the waves. Szantai *et al.* [2011] propose that the waves form near the west Indian coast through a collision between a sea breeze and the easterly/northeasterly offshore flow and that they could be reinforced by the topography [e.g., Zhang and Koch, 2000]. They do not, however, provide substantial direct evidence to support the proposed mechanism because their analysis is limited to satellite observations and 6-hourly ERA-Interim data.

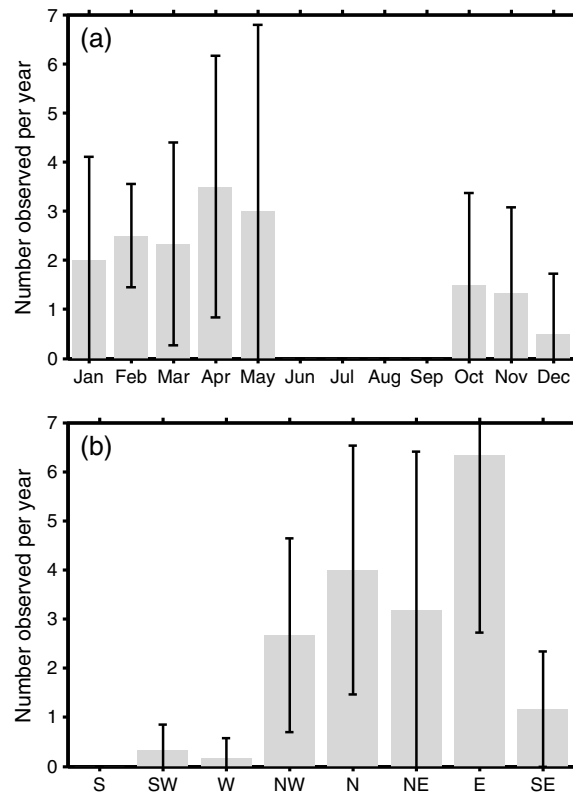


Figure 2. (a) Mean number of wave clouds identified during each month in the Arabian Sea by visible satellite imagery (Meteosat) between 2006 and 2011 and (b) the mean direction of origin. The bars mark plus/minus the standard deviation of the monthly totals for each year.

imagery, (c) high cloud may mask the low-level cloud lines in the satellite imagery, and (d) waves may have been generated that did not produce cloud.

Figure 2a shows the mean number of waves identified from the satellite imagery during each month of the year. Wave clouds are found most frequently between January and May (2–3 per month in a given year) and additionally between October and December (0.5–2 per month in a given year). No waves are identified during the monsoon months (June to September). It is unclear whether this is because no wave clouds are generated during the monsoon or because the waves are obscured by extensive convective cloud.

The mean apparent direction of origin (as determined from the direction of motion) of the wave clouds is shown in Figure 2b. The wave clouds most frequently originate in the east, from the west coast of India (see Figure 4 for a map of locations mentioned in the text). A substantial number also originate from the coasts of Pakistan and Oman, although no wave clouds originate from the south, i.e., from the open ocean, suggesting that the land mass and/or coastline play a role in their formation.

3. Convergence Line Climatology

The wave-cloud lines identified in the climatology of the previous section are, almost certainly, associated with coherent lines of low-level convergence. The aim of the present section is to develop a climatology of convergence lines over the Arabian Sea and surrounding regions.

The method used to identify such convergence lines objectively is a variation on the front-finding algorithm developed by *Berry et al.* [2011]. The method and its application to objectively define the Intertropical Convergence Line are described in detail in *Berry and Reeder* [2014]. In brief, there are four steps in identifying convergence lines. First, the magnitude of the horizontal gradient of the divergence field at 850 hPa is calculated; 850 hPa is approximately the top of the marine stable layer in the Arabian Sea. Second, points at

a similar shape. On 5 and 6 October 2009 separate wave clouds form along several of the coastlines and propagate into the Arabian Sea (Figures 1b and 1c). The waves are most obvious in the 1130 IST imagery, although the waves are also evident at 1730 IST. Identification of the waves in both satellite images allows the direction of travel to be determined. In all cases the waves propagate away from the coast.

A climatology of wave-cloud lines over the Arabian Sea was constructed by examining all visible satellite images available from Meteosat between 2006 and 2011. Wave clouds, such as those illustrated in Figure 1, were identified and the date and propagation direction were recorded. The identification process was purely subjective; close examination of the satellite imagery allowed these types of waves, with their sharp leading edge and following weaker lines, to be distinguished from other types of cloud lines, such as the northwest-southeast orientated cloud lines in the bottom, right-hand corner of Figure 1c. The number of waves detected (Figure 2) is likely to be smaller than the actual number of waves because (a) the satellite spatial and temporal resolution may not have been high enough to identify all the cloud lines, (b) only clouds that occurred during daylight hours could be identified because the clouds do not appear in the infrared satellite

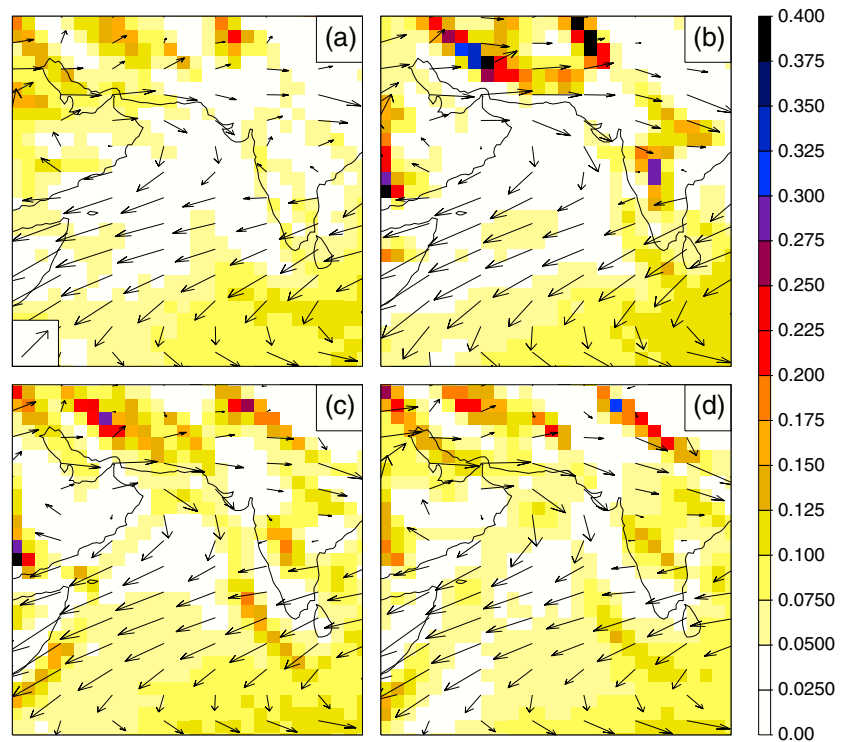


Figure 3. The mean number of convergence lines per day in November–May identified at 850 hPa in the ERA-Interim reanalysis from 1979 to 2009 (shading) and the mean wind at 850 hPa (arrows). (a) The reference arrow in the bottom left corner is 5 m s^{-1} . (a) 1130 IST, (b) 1730 IST, (c) 2330 IST, and (d) 0530 IST.

which the magnitude of the horizontal gradient of the divergence are equal to zero are found. Third, candidate points are identified where the magnitude of the horizontal gradient of the divergence is zero and the divergence is sufficiently negative. Fourth, candidate points satisfying these two criteria are joined using the algorithm outlined in *Berry et al.* [2011]. In essence, points are joined to define a single convergence line if they are sufficiently close and the convergence line is sufficiently long. There are three arbitrary constants in the algorithm: the threshold magnitude of the divergence, the closeness of the candidate points, and the length of the resulting convergence line. These constants are $-2.5 \times 10^{-6} \text{ s}^{-1}$, 3° , and 2 points, respectively, and have been determined through trial and error.

Figure 3 shows the mean number of convergence lines per day at 1130, 1730, 2330, and 0530 IST. The mean wind at 850 hPa is also shown. The convergence line calculations are based on the ERA-Interim reanalysis from 1979 to 2009 at 850 hPa, and the resulting fields are averaged over the months October–May as these are the months in which wave clouds are found in the satellite imagery (Figure 2a). The ERA-Interim reanalysis has a horizontal grid spacing of 1.5° .

At 1130 IST (Figure 3a) there is a very weak maximum of no more than 0.075 lines/day along the west coast of India. As the day proceeds, this maximum increases to about 0.1 lines/per day and moves offshore (Figure 3b). By 2330 IST (Figure 3c) the convergence has strengthened and propagated farther to the southwest. At this time similar maxima are found offshore on all sides of the Arabian Sea. Note that the convergence line maxima peak later in the sequence of panels on the western side of the Arabian Sea because the local time there is only 3 h ahead of UTC compared with 5.5 h ahead on the eastern side. Overnight, these maxima continue to propagate toward the center of the Arabian Sea (Figure 3d). The mean flow is easterly across the Bay of Bengal, southern India, and Somalia, and there is a mean anticyclone over Oman, which causes northwesterly, offshore flow over southern Pakistan. The flow turns cyclonically at low latitudes, becoming westerly over most of the equatorial region.

The climatology of convergence lines derived from the ERA-Interim reanalysis is consistent with that derived from satellite imagery (section 2) even though the reanalysis has relatively coarse horizontal resolution.

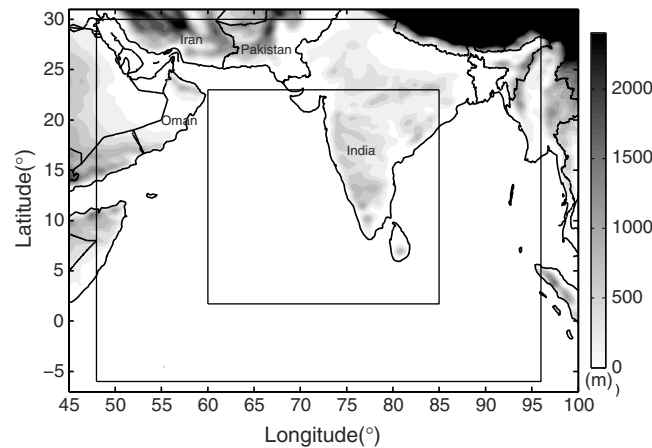


Figure 4. 12 (outer) and 4 (inner) km model nest domains and the locations of countries mentioned in the text. The shading represents orography height (m).

Both show that the dominant propagation directions lie in an arc from northwest to southeast, and both give frequencies in the range 1–5 lines per month. Despite the good agreement between the two climatologies, individual wave-cloud lines identified in the satellite imagery, such as the examples in Figure 1, are not always accompanied by well-defined convergence lines in the ERA-Interim reanalysis. One possible reason may be that the convergence lines are generated very regularly, but relatively few are accompanied by cloud. Consequently, although the convergence lines are greatly under resolved by the ERA-Interim reanalysis and may be too weak to be easily identified on any individual day,

time averaging reinforces the signal. If correct, one implication is that the satellite climatology greatly underestimates the frequency of the convergence lines as only convergence lines that are marked by cloud can be identified.

4. Model Configuration

To determine the formation and propagation mechanism of these wave clouds, a limited area model simulation of a case study is performed with the Met Office Unified Model (MetUM) version 7.3 (Parallel Suite 22). The case illustrated in Figure 1a is chosen because it is one of the most pronounced wave clouds identified in the climatology (section 2); it appears to be similar in structure to the wave clouds reported by *Szantai et al.* [2011], and it propagates toward the west, which is the direction most frequently observed.

The MetUM has a semi-Lagrangian, semi-implicit, and nonhydrostatic formulation and a terrain-following coordinate system [Davies *et al.*, 2005]. Many types of process are parameterized, such as the surface [Essery *et al.*, 2001], the boundary layer [Lock *et al.*, 2000], and mixed-phase cloud microphysics [Wilson and Ballard, 1999]. Convection is parameterized in the global and 12 km nest using the Gregory and Rowntree [1990] scheme. For the 4 km simulations the convection parameterization scheme is effectively switched off.

The model is initialized at 0530 IST, 12 March 2011, and run for 48 h. The global model is initialized using an operational MetUM analysis and is used to create lateral boundary conditions for the nested subdomain with 12 km grid spacing. The 12 km nest then creates lateral boundary conditions and initial conditions for the nested subdomain with 4 km grid spacing. The limits of the 12 and 4 km model domains are illustrated in Figure 4.

5. Wave-Cloud Line Formation Mechanism

Figure 5a shows the mean sea level pressure and wind vectors at 850 hPa at 1730 IST, 12 March 2011, from ERA-Interim [Dee *et al.*, 2011], which is 18 h before the wave was observed off the west coast of India. At this time a region of high pressure is centered over the North Arabian Sea, and a region of low pressure is situated to the southeast of India. The combination of these two systems produces strong low-level easterly winds between Burma/Malaysia (98–102°E, 3–10°N) and the southwest coast of India. In addition, a pronounced trough lies along the west coast of India in the lee of the coastal mountain ranges (orography heights shown in Figure 4). This synoptic situation does not appear in the mean for March 2006–2011 (Figure 5b).

The formation and propagation of the wave-cloud line are illustrated in Figure 6 through plots of 850 hPa vertical velocity and horizontal wind vectors from the 4 km limited area model simulation. The wave forms along the west coast of India between 13 and 18°N (a region where there is strong upward vertical velocity). Between 2130 (Figure 6a) and 0130 IST (Figure 6b) the northeasterly low-level flow accelerates into the lee

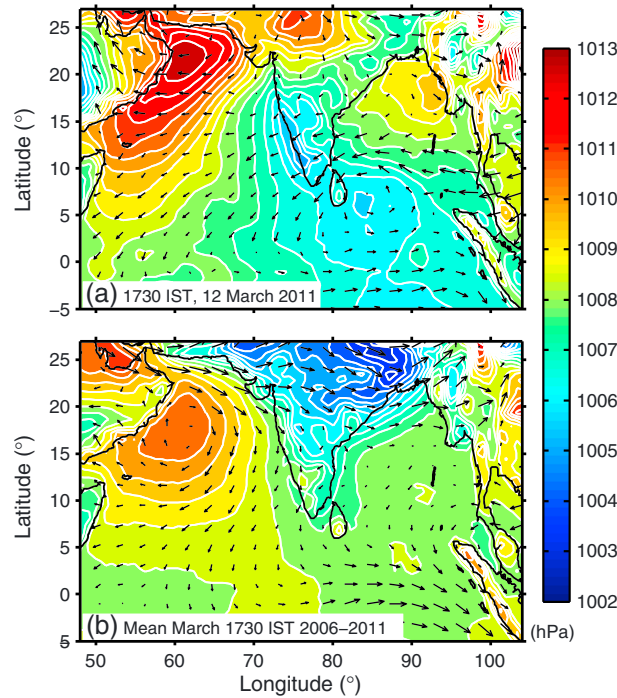


Figure 5. 850 hPa wind (vectors) and mean sea level pressure (shading and contours) from ERA-Interim at (a) 1730 IST, 12 March 2011, and (b) the mean for March at 1200 UTC between 2006 and 2011.

trough, which lies just offshore of the coast, and appears to direct the wave toward the southwest. Presumably, the lee trough is the response to relatively strong easterly flow across the coastal ranges (compare Figures 5a and 5b). The generation and propagation of the wave-cloud line, as represented by the simulated vertical motion, agrees well with the climatological generation and evolution of the convergence lines diagnosed from the ERA-Interim reanalysis. For example, comparing Figure 3c with Figure 6a shows that at this time, the climatological convergence line and the model simulation are similarly located offshore in a west to northwesterly flow. The main difference is that the trough, as marked by the cyclonic turning of the wind, is not well resolved in the climatology.

The wave-cloud line propagates westward (Figures 6c and 6d) ahead of the lee trough, which is itself advancing westward. Figures 6d and 3d show the wave-cloud line in the model simulation and the climatological convergence line at the time of the satellite image in Figure 1a (1130 IST). The location

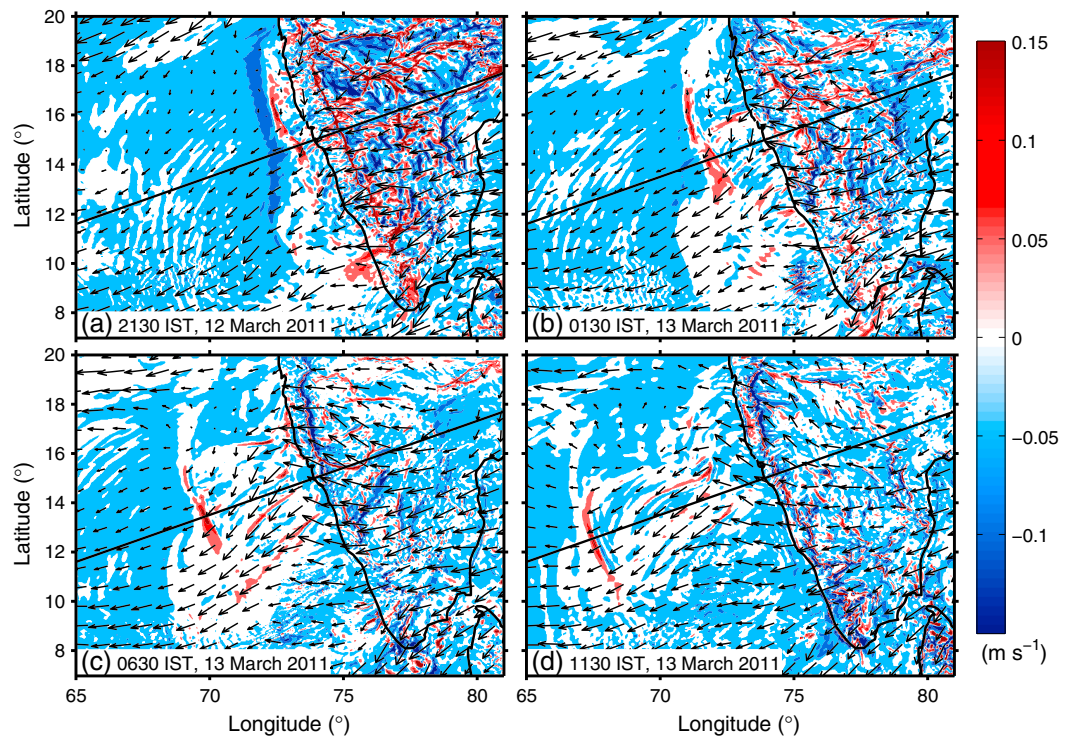


Figure 6. (a–d) 850 hPa vertical velocity (shading) and horizontal wind (vectors). The solid black line marks the diagonal transect used in Figures 7–9.

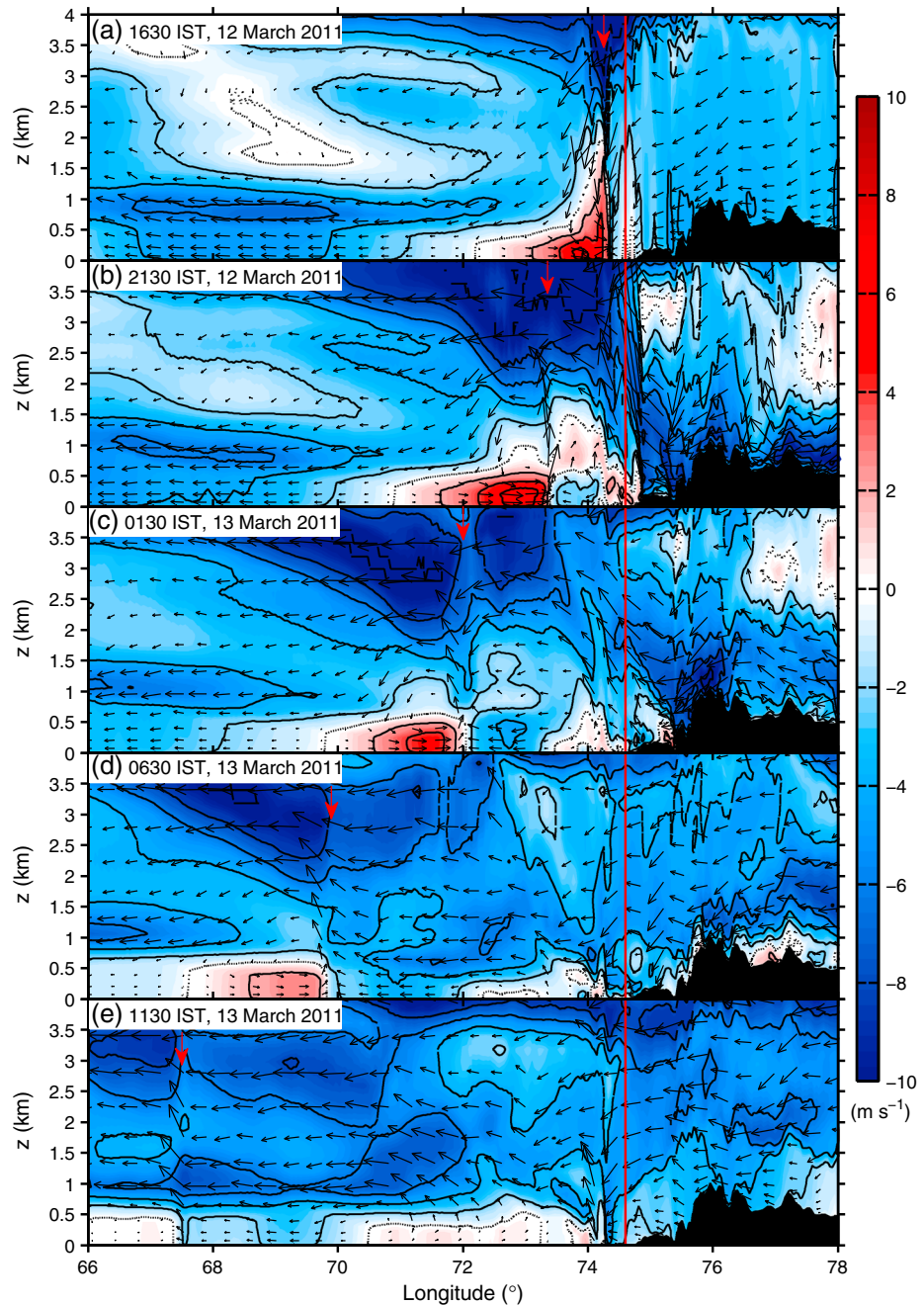


Figure 7. (a–e) Along-transect horizontal wind velocity (shading and black contours, transect marked in Figure 6). The black contours are every 2 m s^{-1} ; the solid black contours represent winds flowing from left to right (southwesterly) and dashed contours represent winds directed from right to left (northeasterly). The wind vectors represent the wind velocity in the vertical plane. The vertical red line marks the location of the coast, and the red arrows the position of the wave.

and horizontal extent of the wave in the model is in good agreement with the observations and in reasonable agreement with the position of the climatological convergence line.

Vertical sections of winds (Figure 7) and virtual potential temperature, θ_v , (Figure 8), are plotted along the diagonal line marked in Figure 6. The strong offshore northeasterly low-level flow is apparent over the mountains and through most of the cross section on both the 12 and 13 March (Figure 7). On the afternoon of the 12 March a southwesterly (onshore) flow forms on the west coast, opposing the synoptic-scale offshore flow (Figure 7a). Although the southwesterlies do not extend inland, this thermally forced circulation is

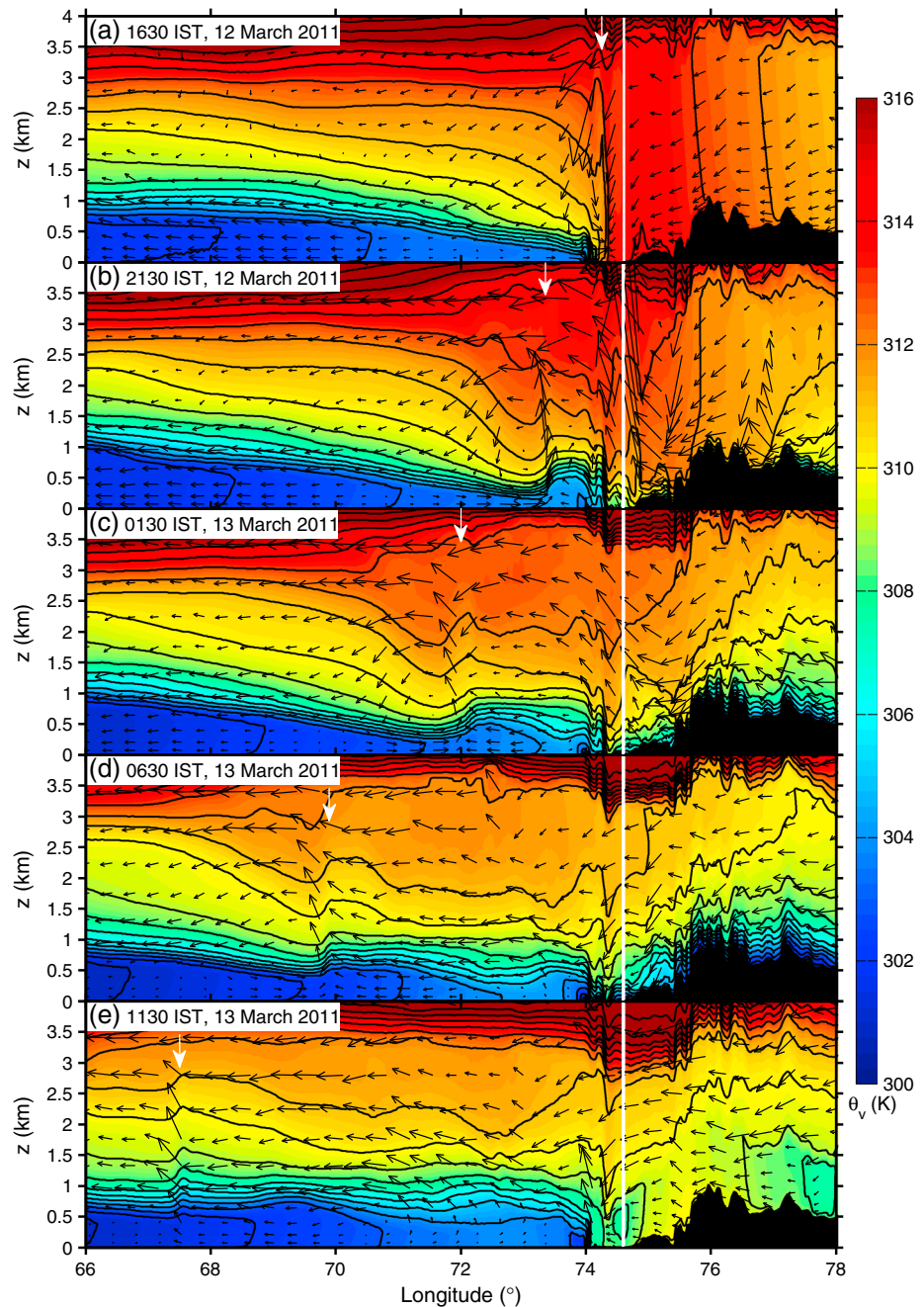


Figure 8. (a–e) θ_v (shading and black contours) and winds (vectors) along the diagonal transect marked in Figure 6. The black contours are every 1 K. The wind vectors represent the horizontal wind in the plane of the cross section, along with the vertical wind. The vertical white line marks the location of the coast, and the white arrows the position of the wave.

dynamically the same as a sea breeze, and for this reason the circulation is called a sea breeze hereafter. Strong upward vertical motion occurs where the two flows meet at 74.5°E with compensating downward vertical motion just southwest of this at 73.7°E.

The easterly flow over the mountains accelerates during the night of the 12 March (Figures 7b and 7c) and begins to push the sea breeze back, over the ocean and into the marine boundary layer (Figure 7b). The acceleration of the easterly flow may be due to nighttime downslope winds from the mountains or be simply due to the reduction in drag associated with the cessation of daytime convection. The convergence zone continues to move toward the southwest, until the opposing flow from the sea breeze subsides (Figure 7d and 7e).

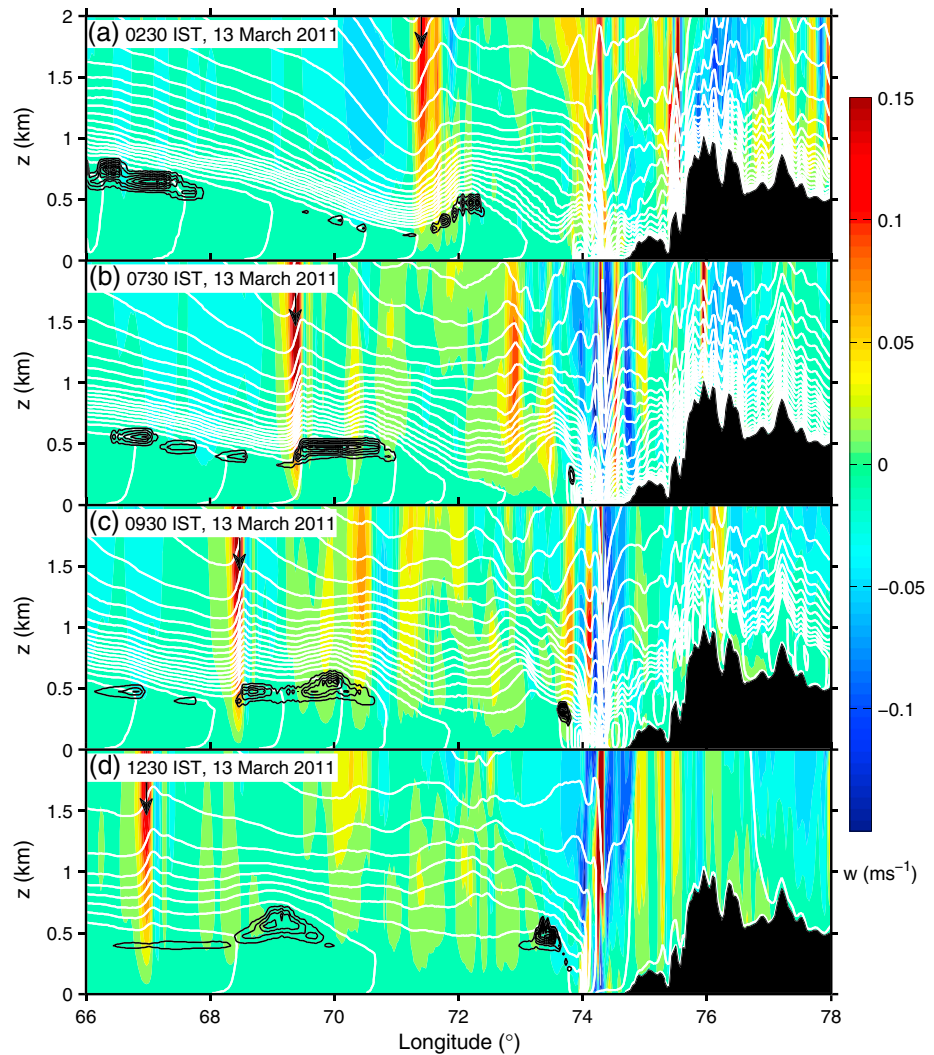


Figure 9. (a–d) Vertical velocity (shading), θ_v (white contours), and liquid cloud water (black contours) along the diagonal transect marked in Figure 6. The white contours are every 1 K, and black arrows mark the position of the wave.

Figure 8 shows the propagation of the wave to the southwest in terms of θ_v . Over the ocean the boundary layer is well mixed and capped with an inversion between approximately 0.7 and 1.2 km above the surface. Over the mountains the boundary layer is well mixed up to 3.5 km during the day, although it becomes more stable, especially in the valleys, overnight. The upward vertical velocity within the coastal convergence zone lifts the capping inversion by up to 500 m from its original position (73.5°E, Figure 8b), while the downward vertical velocity ahead of the wave lowers the height of the inversion by several hundred meters (73.0°E, Figure 8b). As the system propagates toward the southwest, the circulation ahead of the wave weakens until only the upward motion is significant (Figure 8d and 8e).

Cloud forms immediately behind the region of vertical velocity associated with the leading edge of the wave. Cloud first appears at 2330 IST, 13 March, and develops as the wave propagates southwestward (Figures 9a and 9b). It resides at the top of the boundary layer, within the horizontal section that has been elevated by the wave. It is this cloud which makes the waves visible in the satellite imagery in Figure 1a. At 0930 IST the wave becomes detached from the main cloudy region and is approximately 1.5° ahead of it by 1230 IST (Figures 9c and 9d).

The propagation speed of the wave can be computed from a Hovmöller plot (Figure 10) of vertical velocity at 1.5 km above the surface along the diagonal transect marked in Figure 6. The speed of the wave is reasonably

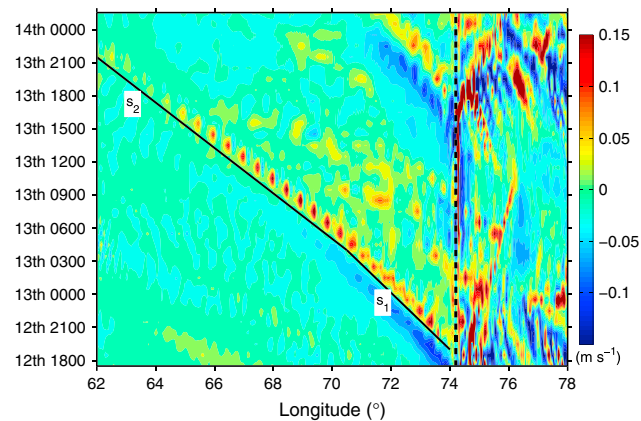


Figure 10. Hovmöller plot of vertical velocity at 1500 m above the surface along the diagonal transect marked in Figure 6. Times are in IST during March 2011. The black dashed line marks the location of the coast in the diagonal transect, and s_1 and s_2 indicate the two speeds of the wave.

marked by the jump in the isentropes at about 73° and the rarefaction is the region immediately to the west where the isentropes are depressed. As the environmental flow is westerly, both the rarefaction and the jump propagate to the west. Hammack and Segur [1974, Figure 8] show that the jump evolves into a solitary wave, which overtakes the waves of depression. Presumably, this is the transition in the speed of the wave cloud identified at about 71° in Figure 10. Physically, the acceleration is related to the depth of the marine boundary layer ahead of the disturbance (Figure 8). The rarefaction is associated with a shallow stable layer, whereas the solitary wave that overtakes it propagates on a deeper stable layer. Thereafter, the wave speed remains constant until it decays at approximately 62°E at 2200 IST, 13 March 2011. The lifetime of the wave is at least 30 h.

6. Conclusions

There are very few climatologies of convergence lines or of large amplitude waves and their associated cloud lines. Climatologies of wave-cloud lines and convergence lines over the Arabian Sea have been constructed and compared. The former was based on all Meteosat visible satellite images between 2006 and 2011, whereas the latter was based on the ERA-Interim reanalysis 850 hPa wind field from 1979 to 2009 and used the method developed in Berry and Reeder [2014]. Although the ERA-Interim reanalysis has relatively coarse horizontal resolution, the climatology of convergence lines derived from it was consistent with that for the wave-cloud lines identified in the satellite imagery. Both climatologies showed that lines occurred in all months outside of the summer monsoon. In particular, in both climatologies, lines propagated away from the coastlines surrounding the Arabian Sea at a frequency of approximately 1–5 times per month.

The generation mechanism was identified in a simulation with the Met Office Unified Model of a wave-cloud line that formed on 13 March 2011, which was similar in appearance to those observed by Szantai *et al.* [2011]. The model was initialized at 0530 IST, 12 March 2011, and run for 48 h with the grid spacing of the innermost domain equal to 4 km. In the afternoon, a southwesterly sea breeze developed along the western coastline of India. This sea breeze was opposed by synoptic-scale northeasterly flow. As the daytime turbulence decayed and the boundary layer stabilized, the low-level northeasterly flow across India accelerated in the late evening and early hours of the morning, pushing the leading edge of the sea breeze offshore. It appears that the acceleration may have been aided by nocturnal downslope winds. As the northeasterly flow pushed against the marine inversion, cold air accumulated, both deepening the marine layer and producing a wave that propagated to the west on the marine inversion. Ascent at the leading edge of the wave produced cloud in the simulation similar to that observed. The generation mechanism for wave-cloud lines over the Arabian Sea appears to be very similar to that documented by Birch and Reeder [2012] for wave-cloud lines that develop off northwestern Australia.

constant at $11.8 \pm 1 \text{ m s}^{-1}$ as it travels from the coast to 71°E (s_1) and then accelerates to an approximately constant speed of $15.2 \pm 1 \text{ m s}^{-1}$ (s_2).

The evolution and speed of the wave cloud appear to have much in common with the evolution of a large amplitude wave of depression. A wave of depression is formed as the offshore easterly flow pushes the marine stable layer downward to the west of the eastern edge of the sea breeze circulation. According to theory based on the Korteweg de Vries equation, waves of depression comprise of both waves of rarefaction and compression [e.g., Hammack and Segur, 1974]. Figure 8 shows both these features. For example, in Figure 8b the wave of compression is

Acknowledgments

The model data used in this study is available from the corresponding author. We are grateful for help from National Centre for Atmospheric Science Computer Model Support (NCAS-CMS) for providing model analyses and assistance with model issues. This work made use of the facilities of HECToR, the UK's national high-performance computing service, which is provided by UoE HPCx Ltd. at the University of Edinburgh, Cray Inc., and NAG Ltd., and funded by the Office of Science and Technology through EPSRC's High End Computing Program. We would like to thank the Dundee Satellite Receiving Station for providing the Meteosat imagery. C.E.B was funded by NERC grant NE/G018499/1 and G.J.B is funded through the ARC Super Science Fellowship FS100100081. Finally, we would like to thank Roger Smith for his insightful review.

References

- Berry, G. J., and M. J. Reeder (2014), Objective identification of the intertropical convergence zone: Climatology and trends from the ERA-Interim reanalysis, *J. Clim.*, *27*, 1894–1909, doi:10.1175/JCLI-D-13-00339.1.
- Berry, G. J., M. J. Reeder, and C. Jakob (2011), A global climatology of atmospheric fronts, *Geophys. Res. Lett.*, *38*, L04809, doi:10.1029/2010GL046451.
- Birch, C. E., and M. J. Reeder (2012), Wave-cloud lines over northwest Australia, *Q. J. R. Meteorol. Soc.*, *139*, 1311–1326, doi:10.1002/qj.2043.
- Bosart, L. F., and F. Sanders (1986), Mesoscale structure in the megalopolitan snowstorm of 11–12 February 1983, Part III: A large-amplitude gravity wave, *J. Atmos. Sci.*, *43*, 924–939.
- Bosart, L. F., W. E. Bracken, and A. Seimon (1998), A study of cyclone mesoscale structure with emphasis on a large-amplitude inertia-gravity wave, *Mon. Weather Rev.*, *126*, 1497–1527.
- Christie, D. R. (1992), The morning glory of the Gulf of Carpentaria: A paradigm for non-linear waves in the lower atmosphere, *Aust. Met. Mag.*, *41*, 21–60.
- Christie, D. R., and K. L. Muirhead (1983), Solitary waves: A hazard to aircraft operating at low altitudes, *Aust. Met. Mag.*, *31*, 97–109.
- Clarke, R. H. (1972), The morning glory: An atmospheric hydraulic jump, *J. Appl. Meteorol.*, *11*, 304–311.
- Clarke, R. H., R. K. Smith, and D. G. Reid (1981), The Morning Glory of the Gulf of Carpentaria: An atmospheric undular bore, *Mon. Weather Rev.*, *109*, 1726–1750.
- da Silva, J. C. B., and J. M. Magalhães (2009), Satellite observations of large atmospheric gravity wave in the Mozambique channel, *Int. J. Rem. Sens.*, *30*, 1161–1182.
- Davies, T., M. J. P. Cullen, A. J. Malcolm, M. H. Mawson, A. Staniforth, A. A. White, and S. Wood (2005), A new dynamical core for the Met Office's global and regional modelling of the atmosphere, *Q. J. R. Meteorol. Soc.*, *131*, 1759–1782.
- Dee, D. P., et al. (2011), The ERA-Interim reanalysis: Configuration and performance of the data assimilation system, *Q. J. R. Meteorol. Soc.*, *137*, 553–597.
- Essery, R. L. H., M. J. Best, and P. M. Cox (2001), MOSES 2.2 technical documentation, *Tech. Rep.*, Met Office, 14 Aug.
- Goler, R. A., and M. J. Reeder (2004), The generation of the morning glory, *J. Atmos. Sci.*, *61*, 1360–1376.
- Gregory, D., and P. R. Rowntree (1990), A mass flux convection scheme with representation of cloud ensemble characteristics and stability-dependent closure, *Mon. Weather Rev.*, *118*, 1483–1506.
- Hammack, J. L., and H. Segur (1974), The Korteweg-de Vries equation and water waves, Part 2. Comparison with experiments, *J. Fluid Mech.*, *65*, 289–314.
- Koch, S. E., and R. E. Golus (1988), A mesoscale gravity wave event observed during CCOPE, Part I: Multiscale statistical analysis of wave characteristics, *Mon. Weather Rev.*, *116*, 2527–2544.
- Koch, S. E., W. Feltz, F. Fabry, M. Pagowski, B. Geerts, K. M. Bedka, D. O. Miller, and J. W. Wilson (2008), Turbulent mixing processes in atmospheric bores and solitary waves deduced from profiling systems and numerical simulation, *Mon. Weather Rev.*, *136*, 1373–1400.
- Lock, A. P., A. R. Brown, M. R. Bush, G. M. Martin, and R. N. B. Smith (2000), A new boundary layer mixing scheme, Part I: Scheme description and single-column model tests, *Mon. Weather Rev.*, *128*, 3187–3199.
- Mapes, B. E. (1993), Gregarious tropical convection, *J. Atmos. Sci.*, *50*, 2026–2037.
- Neal, A. B., and I. J. Butterworth (1973), The recurring cloud line in the Gulf of Carpentaria, *Working Paper*, *163*, Bur. Met., Australia.
- Nudelman, I., R. K. Smith, and M. J. Reeder (2010), A climatology of pressure jumps around the Gulf of Carpentaria, *Aust. Meteor. Ocean. J.*, *60*, 91–102.
- Powers, J. G., and R. J. Reed (1993), Numerical simulation of large-amplitude mesoscale gravity-wave event of 15 December 1987 in the central United States, *Mon. Weather Rev.*, *121*, 2285–2308.
- Reeder, M. J., and R. K. Smith (1998), Mesoscale meteorology, *Meteorol. Mono.*, *27*, 201–241.
- Reeder, M. J., R. K. Smith, J. R. Taylor, D. J. Low, S. J. Arnup, L. Muir, and G. Thomsen (2013), Diurnally-forced convergence lines in the Australian tropics, *Q. J. R. Meteorol. Soc.*, doi:10.1002/qj.2021.
- Smith, R. K. (1986), Evening glory wave-cloud lines in northwestern Australia, *Aust. Met. Mag.*, *34*, 27–33.
- Szantai, A., P. Drobinski, and F. Désalmand (2011), Dynamics of solitary waves observed over the North Indian Ocean during the Indian Ocean Experiment (INDOEX) 1999, *J. Geophys. Res.*, *116*, D05115, doi:10.1029/2010JD014877.
- Wilson, D. R., and S. P. Ballard (1999), A microphysically based precipitation scheme for the U.K. Meteorological Office Unified Model, *Q. J. R. Meteorol. Soc.*, *125*, 1607–1636.
- Zhang, F., and S. E. Koch (2000), Numerical simulations of a gravity wave event over CCOPE, Part II: Waves generated by an orographic density current, *Mon. Weather Rev.*, *128*, 2777–2796.
- Zheng, Q., X.-H. Yan, W. T. Liu, V. Klemas, D. Greger, and Z. Wang (1998), A solitary wave packet in the atmosphere observed from space, *Geophys. Res. Lett.*, *25*, 3559–3562, doi:10.1029/98GL02319.